Acta Biomaterialia 10 (2014) 5064–5073

Contents lists available at ScienceDirect

Acta Biomaterialia

journal homepage: www.elsevier.com/locate/actabiomat

Strain rate hardening: A hidden but critical mechanism for biological composites?

Ravi Kiran Chintapalli, Stephanie Breton, Ahmad Khayer Dastjerdi, Francois Barthelat *

Department of Mechanical Engineering, McGill University, 817 Sherbrooke Street West, Montreal, QC H3A 2K6, Canada

ARTICLE INFO

Article history:
Received 4 March 2014
Received in revised form 3 July 2014
Accepted 23 August 2014
Available online 29 August 2014

Keywords:
Biological composites
Strain hardening
Strain rate hardening
Staggered composites
Micromechanics

ABSTRACT

Natural materials such as nacre, bone, collagen and spider silk boast unusual combinations of stiffness, strength and toughness. Behind this performance is a staggered microstructure, which consists of stiff and elongated inclusions embedded in a softer and more deformable matrix. The micromechanics of deformation and failure associated with this microstructure are now well understood at the "unit cell" level, the smallest representative volume for this type of material. However, these mechanisms only translate to high performance if they propagate throughout large volumes, an important condition which is often overlooked. Here we present, for the first time, a model which captures the conditions for either spreading of deformations or localization, which determines whether a staggered composite is brittle or deformable at the macroscale. The macroscopic failure strain for the material was calculated as function of the viscoplastic properties of the interfaces and the severity of the defect. As expected, larger strains at failure can be achieved when smaller defects are present within the material, or with more strain hardening at the interface. The model also shows that strain rate hardening is a powerful source of large deformations for the material as well, a result we confirmed and validated with tensile experiments on glass–polydimethylsiloxane (PDMS) nacre-like staggered composites. An important implication is that natural materials, largely made of rate-dependent materials, could rely on strain rate hardening to tolerate initial defects and damage to maintain their functionality. Strain rate hardening could also be harnessed and optimized in bio-inspired composites in order to maximize their overall performance.

1. Introduction

High-performance natural materials such as nacre, teeth, bone and spider silk boast outstanding combinations of stiffness, strength and toughness which are currently not possible to achieve in engineering materials. For example, dragline silk from spiders surpasses the strength and toughness of the most sophisticated engineering steels [1], while collagenous tissues such as bone, tendons or fish scales display powerful toughening mechanisms over multiple length scales [2,3]. Nacre from mollusk shells is 3000 times tougher than the brittle mineral it is made of [4], and it is the toughest materials amongst other mollusks shell materials [5] and other highly mineralized stiff biological materials such as tooth enamel [6]. An examination of the structure and mechanics of these materials reveals a "universal" structural pattern consisting of stiff and hard inclusions embedded in a softer but more deformable matrix. The inclusions are elongated and are parallel to each other, and aligned with the direction of loading (Fig. 1). This structure is particularly well suited to uniaxial or biaxial tensile loads [7]. In one-dimensional fibers and "ropes" such as spider silk or tendons, uniaxial tension is the only loading configuration. More "bulky" materials, such as nacre and bone, undergo multi-axial loading modes but, since these materials are quasi-brittle, tensile stresses are always the most dangerous stresses. Increasing tensile strength is therefore critical to the performance of these materials. The fundamental mechanism of tensile deformation is the gliding or sliding of the inclusions on one another. In this mechanism the inclusions remain linear-elastic, but the interface dissipates a large amount of energy through viscous deformation. The resulting stress–strain curves display relatively large deformation before failure [8,9] and, as a result, the material can absorb a tremendous amount of mechanical energy (area under the stress–strain curve). Energy absorption is a critical property for materials like bone, nacre and spider silk, which must absorb energy from impacts without fracturing. Interestingly, the staggered structure has recently been shown to be the most efficient in generating optimum combinations of stiffness, strength and energy absorption [10,11].

* Corresponding author. Tel.: +1 514 398 6318.
E-mail address: francois.barthelat@mcgill.ca (F. Barthelat).

http://dx.doi.org/10.1016/j.actbio.2014.08.027
1742-7061/

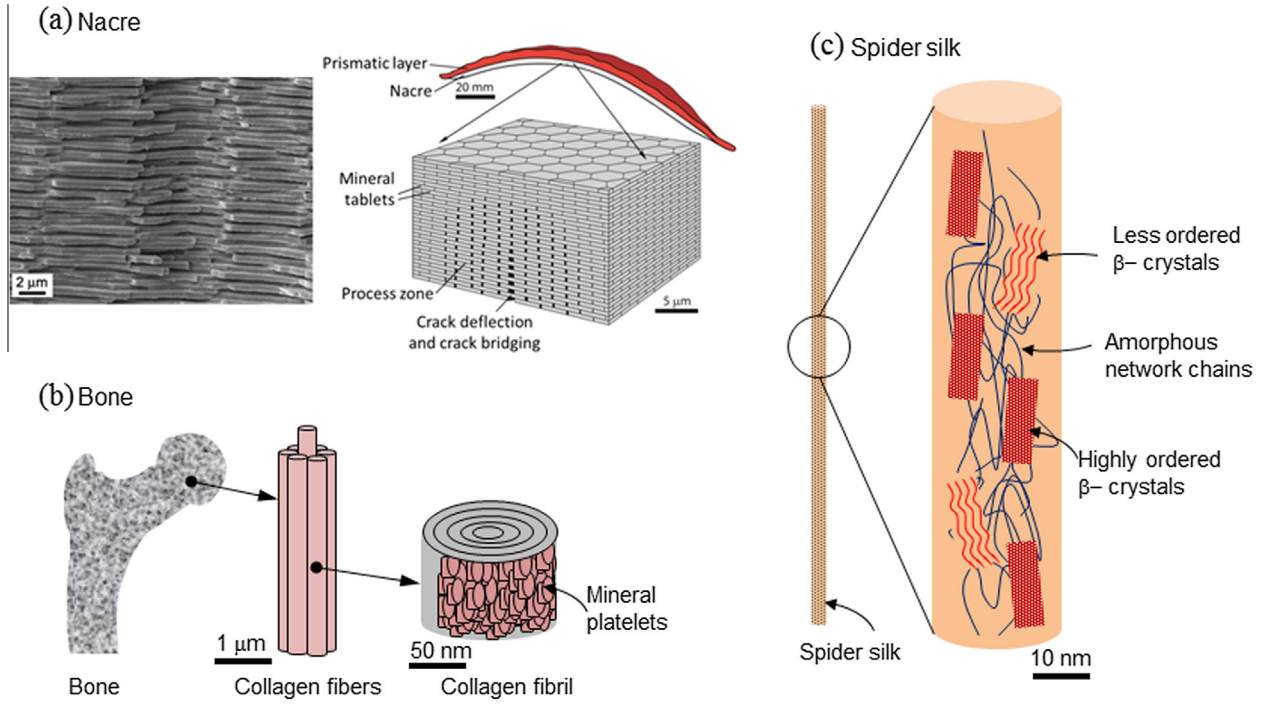

Fig. 1. Examples of staggered composites in nature: (a) nacre, (b) bone, (c) spider silk.

The sliding mechanism of the inclusions was observed experimentally in nacre and bone using direct imaging methods or X-ray diffraction [8,12,13]. This mechanism was also captured in models using closed-form solutions and finite elements [10,14–17]. These models can predict the modulus, strength and energy absorption as functions of the properties of the constituents and the morphology of the microstructure (aspect ratio of the inclusions, arrangement and interface thickness). Materials such as nacre and collagen fibrils display remarkable periodicities at the nano- and microscales, and therefore the general approach for micromechanical models is usually based on the mechanical response of a periodic unit cell. This "representative volume element" (RVE) approach greatly simplifies computations, and it is based on the assumption that the mechanics and properties of the unit cell are representative of the entire material. However, the powerful mechanisms observed at the unit cell level can translate to the macroscale only if these mechanisms spread over large volumes within the material, which requires some type of hardening mechanism (Fig. 2). When a material is deformed, nonlinear deformations may accumulate near initial defects, flaws and other stress concentrators within the material. A hardening mechanism ensures that further deformations within these regions require an increasing amount of stress, so that other regions of the material may also start accumulating nonlinear deformations. Hardening mechanisms therefore promote the spreading of nonlinear deformations, and maximize the effect of beneficial mechanisms such as energy dissipation. Without some type of hardening mechanism, the benefits of nonlinear deformations would be confined to small volumes within the material. In this localization scenario, a unit cell taken within the defect region behaves differently from a unit cell outside of the defect region, so that the assumption of the unit cell being representative of the material breaks down. In effect, high strain concentration and early localization lead to small macroscale strain and to a brittle mechanical response for the material (Fig. 2).

The sliding mechanism of the inclusions on one another also has implications in terms of fracture mechanics. If the interfaces between the inclusions are sufficiently weak, propagating cracks will be deflected and will circumvent the inclusions. The subsequent pullout of the inclusions produces toughening by way of crack bridging, the tablets exerting a closure force on the crack faces. In a material like nacre, however, it was demonstrated that bridging only provides a small fraction of the overall toughness [11], a larger portion of toughening coming from the spreading of nonlinear deformations over large volumes. This mechanism dissipates a tremendous of energy, which contributes to the toughness

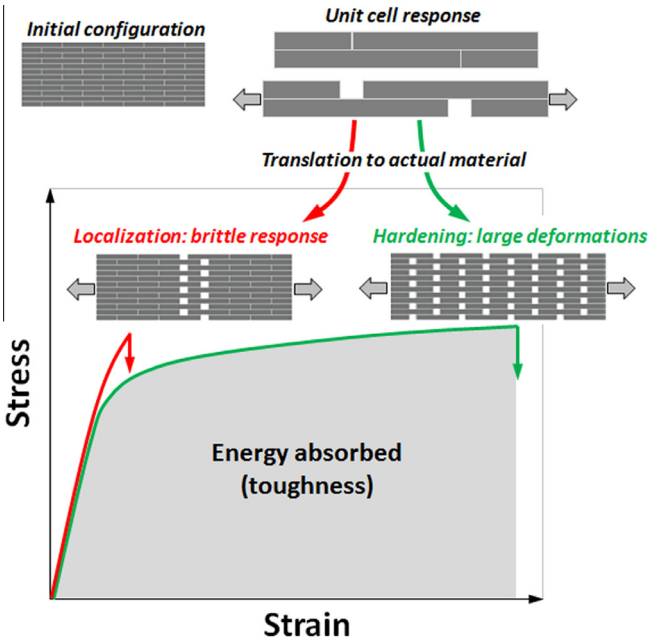

Fig. 2. Strain concentration and localization in staggered composites leads to brittle behavior. Spreading of deformation leads to higher strain and energy absorption (which generates toughness).

of the material [11]. Here again, the formation of a large process zone around propagating cracks relies on some type of hardening mechanism in the material. In summary, even if the mechanisms of tablet sliding is optimized and produces attractive properties at the level of the unit cell, these mechanisms will only translate to a poor material if they do not propagate throughout the material.

In natural nacre, an important mechanism for the spreading of nonlinear deformations is associated with the microscopic waviness of the inclusions, which generates progressive locking and "geometric strain hardening" at the local scale [16]. However, in other material systems, such as collagen fibrils and spider silk, the inclusions are relatively flat and do not display any waviness, and the origin of hardening and large deformations in these materials therefore remains elusive. Some of the proteins present at the interfaces of nacre or bone show remarkable deformation mechanisms and large deformations [18,19], but it is unclear whether these proteins can produce enough strain hardening to translate to large deformations at the macroscale. What is known, however, is that that the proteins and biopolymeric matrices found in natural materials are rate sensitive, exhibiting viscoelastic and viscoplastic responses [20–22].

In this work we explore the idea that strain rate hardening at the interfaces in biological materials can be a powerful mechanism for generating large inelastic deformations and high material performance. Strain rate hardening materials require more stress to deform at higher rates of deformations, with implications on spreading deformation which are similar to strain hardening. When a concentration of strain appears at initial defects, the rate of deformation increases faster than in the rest of the material, which in turn requires more stress. As a result, other regions of the material will also accumulate nonlinear deformations, which then spread over large volumes. Strain rate hardening has already been demonstrated, theoretically and experimentally, to be a potent mechanism to delay necking instabilities in ductile metals [23–25].

In this work, the conditions for large deformations in staggered composites are derived, incorporating the effects of strain hardening and strain rate hardening at the interfaces. The effects of strain rate hardening are then illustrated and verified with a "model material" made of staggered hexagonal glass plates bonded by an ultraviscous Newtonian fluid.

2. Representative volume element modeling: viscoplastic response

The shear-tension model shown on Fig. 3, based on shear lag models for composites [26], is typically used to predict the mechanical response of biological and biomimetic composites [14,15]. In this two-dimensional model, the inclusions (referred to hereinafter as "tablets", to be consistent with the terminology used for nacre) are aligned with the direction of loading, and as a result they carry stress in tension while the interfaces undergo shear stresses and channel the loads between tablets. For simplicity, we focus on the case where the tablets overlap over half of their length. The tablets are modeled as linear-elastic and the interface is modeled as linear elastic or as elastic-perfectly plastic [15]. Here we consider a more general case where the interfaces are made of a viscoplastic material with rate dependence which follows the general constitutive equation [27]:

$$\tau = K\gamma^{m}\dot{\gamma}^{n} \tag{1}$$

In Eq. (1), τ and γ are the true shear stress and true shear strain at the interface, and $\dot{\gamma}$ denotes the time derivative of the shear strain, or the shear strain rate. K is the strength index, m is the strain hardening coefficient and n is the strain rate sensitivity (K, m and n are material properties). This general model can capture strain hardening as well as rate effects, and it can capture the behavior of a large variety of materials, including plastic solids and rheological fluids. The tablets are typically much stiffer than the interfaces, and therefore they are modeled as rigid. This assumption is reasonable, considering that the inclusions in biological and biomimetic composites are typically at least one order of magnitude stiffer than the interface (the assumption of rigid tablets will also be verified in the experimental section). A direct implication of this assumption is that the distribution of shear stress and shear strain along the interface is uniform [28], and that the only non-zero strain at the interface is the shear strain γ. As the tablets slide and pull out, and as the relative sliding of the tablets u/L increases, the load-carrying surface of the tablets decreases. The viscoplastic interfaces flow to accommodate this effect and maintain the cohesion between tablets, albeit over a reduced length $L-u$ (Fig. 3b). This geometric softening is similar to the reduction of the load-bearing area from plastic deformations occurring in metals under tension.

The overall tensile stress is then simply given by considering the equilibrium of a half-tablet. The tensile force carried by each the tablet is:

$$F = 2(L-u)\tau \tag{2}$$

where F is the tensile force, $2L$ is the length of the tablet, u is the sliding distance at each interface and τ is the shear stress transmitted through each interface. The macroscopic tensile stress per unit width of the composite is then

$$\sigma = \frac{F}{2(t_t + t_i)} \tag{3}$$

where t_t and t_i are the thicknesses of the tablets and interfaces. Using the volume fraction of the tablets $\phi = \frac{t_t}{(t_t+t_i)}$ $(0<\phi<1)$, the overlap ratio of the tablets $\rho = \frac{L}{t_t}$ $(\rho>0)$) and the average shear stress per unit width at the interface $\tau = \frac{F}{L}$, Eqs. (2) and (3) become:

$$\sigma = \phi\rho\left(1-\frac{u}{L}\right)\tau \tag{4}$$

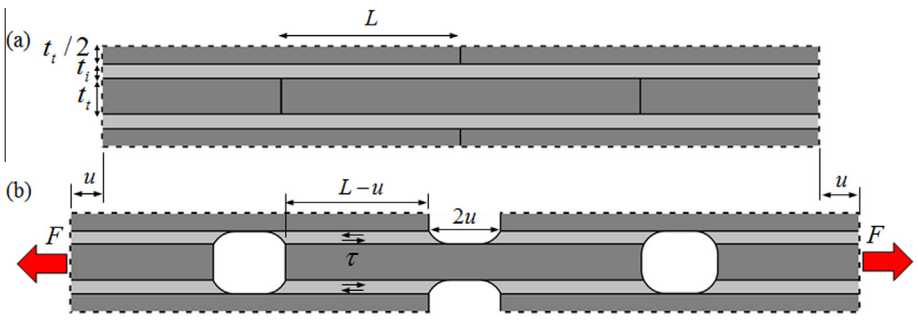

Fig. 3. RVE (a) at rest and (b) deformed in tension.

Meanwhile, the deformation of the RVE can be easily captured, recalling that tablets are considered rigid and that the interfaces are in a state of uniform simple shear. The true shear strain is given simply by:

$$\gamma = \frac{u}{t_i} \tag{5}$$

In order to characterize the tensile deformation of the RVE, we use the engineering strain definition (true strains could have also been used, without changing the main results of the model). Since the tablets are assumed to be rigid, the tensile strain of the RVE is then written as:

$$\varepsilon = \frac{u}{L} = \frac{t_i}{L}\gamma = \left(\frac{1-\phi}{\phi}\right)\frac{1}{\rho}\gamma \tag{6}$$

Combining Eqs. (4) and (5), we can also write the stress as:

$$\sigma = \phi\rho(1-\varepsilon)\tau \tag{7}$$

To model the tensile response of a material deformed at a constant rate, we write the strain as $\varepsilon = \dot{\varepsilon}t$, where $\dot{\varepsilon}$ is the constant macroscopic tensile strain rate imposed on the material and t denotes time. Combining Eqs. (1), (6) and (7) gives the general mechanical response of the RVE:

$$\sigma = K\phi\left(\frac{\phi}{1-\phi}\right)^{m+n}\rho^{m+n+1}(1-\varepsilon)\varepsilon^m\dot{\varepsilon}^n \tag{8}$$

Eq. (8) shows that macroscale tensile stress results from two competing effects: an intrinsic material effect where the interface produces more stress as deformation is increased and a geometrical softening effect where the tablets lose contact as deformation increases. To illustrate this result, Fig. 4 shows the qualitative response of the RVE with three different types of materials at the interface. For the cases where $m = 0$ (no material strain hardening), the geometric softening effect always prevails and the stress decreases linearly with strain until the tablets lose contact at $\varepsilon = 1$. This case includes rate-independent plastic solids ($n = 0$) and viscous fluids (for $n > 0$). When strain hardening is present at the interface ($m > 0$ and $n \geqslant 0$), strain hardening at the RVE level initially prevails until a maximum value for stress, after which softening from the geometric effects overcome material effects. This case corresponds to a strain hardening solid with rate dependence (if $n > 0$) or with rate-independent plasticity (if $n = 0$).

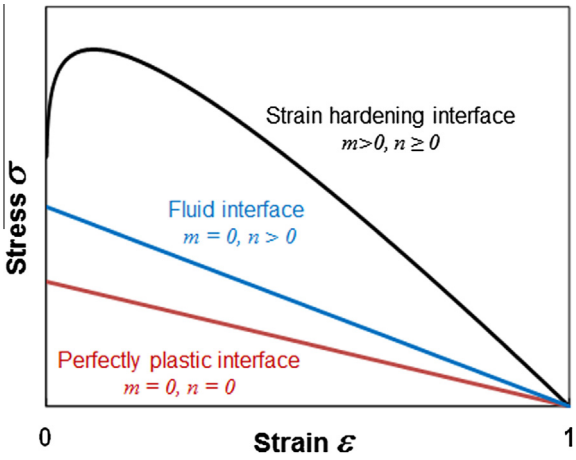

Fig. 4. Qualitative response of an RVE with different types of materials at the interface.

3. Modeling real materials: strain concentration and localization at pre-existing defects

The model presented in the previous section assumes that a single microstructural element, or unit cell, is representative of the entire material. This assumption is typically made to model nacre, bone and other similar natural or biological materials [14,15]. In reality, these materials contain defects which can raise stresses locally and generate strain concentrations, which may eventually turn into localization, large cracks and macroscopic brittle behavior. In the event where strain concentration or localization occurs, using a simple unit cell as an RVE is not appropriate since the deformations in the defect region have become significantly larger than anywhere else in the material. Localization and failure may be delayed by strain hardening, as seen in the previous section, but the single-cell RVE model also shows how softening rapidly prevails when large deformations are considered. In this section, we capture the strain concentration at defects by considering a larger RVE which is made of a chain of N unit cell models, where $N \gg 1$ for a typical material (Fig. 5). The RVE contains a defect, which we model as a region where the overlap between the tablets is smaller than everywhere else in the material ($L_0 < L$). The RVE is periodic along the vertical direction (across the direction of the tablets) so that the defect it contains actually represents a line defect within the material. This approach to capturing the effect of strain concentration is similar to models previously developed to predict the onset of instability due to necking in metals [23,24]. As a result of the defect, stretching the model by a macroscopic strain ε will result in tensile strains $\varepsilon_0 > \varepsilon$ in the defect region (Fig. 5b). When stretching is continued, the material eventually fails at the defect (Fig. 5c), where the tablet is entirely pulled out and $\varepsilon_0 = 1$. The strain in the rest of the material is then $\varepsilon_{max} < 1$, and represents its macroscopic strain at failure ε_{max}. ε_{max} can therefore be used as a measure of the brittleness or ductility of the material. The objective of this model is now to predict ε_{max} as a function of the severity of the defect and of the material behavior at the interface.

We first define the overlap ratios:

$$\rho_0 = \frac{L_0}{t_t} \quad \text{and} \quad \rho = \frac{L}{t_t} \tag{9}$$

The relative difference of overlap lengths between the defect and the rest of the material provides a non-dimensional measure of the severity of the defect, which is written:

$$\eta = \frac{\rho - \rho_0}{\rho} \quad \text{with } 0 \leqslant \eta \leqslant 1 \tag{10}$$

In Eq. (10), $\eta = 0$ represents a material with no defect and $\eta = 1$ represents the extreme case where the defect splits the material before it is even loaded. For continuity of tensile stress between the defect and the rest of the material, one must have:

$$\sigma_0 = \sigma \text{ or } (L_0 - u_0)\tau_0 = (L-u)\tau \tag{11}$$

where τ_0 is the shear stress at the interface in the defect region and τ is the shear stress in the rest of the interfaces. The engineering tensile strains in each of the regions are given by:

$$\varepsilon_0 = \frac{u_0}{L_0} \quad \text{and} \quad \varepsilon = \frac{u}{L} \tag{12}$$

Combining Eqs. (11) and (12) gives:

$$(1-\varepsilon_0)\tau_0 = \frac{1}{1-\eta}(1-\varepsilon)\tau \tag{13}$$

Note that initially, the deformations are small and $\varepsilon \approx \varepsilon_0 \approx 0$, so that $\tau_0 \approx \frac{1}{1-\eta}\tau$, and therefore $\tau_0 \geqslant \tau$. As expected, yielding and flow will therefore occur first at the interfaces located at the defect.

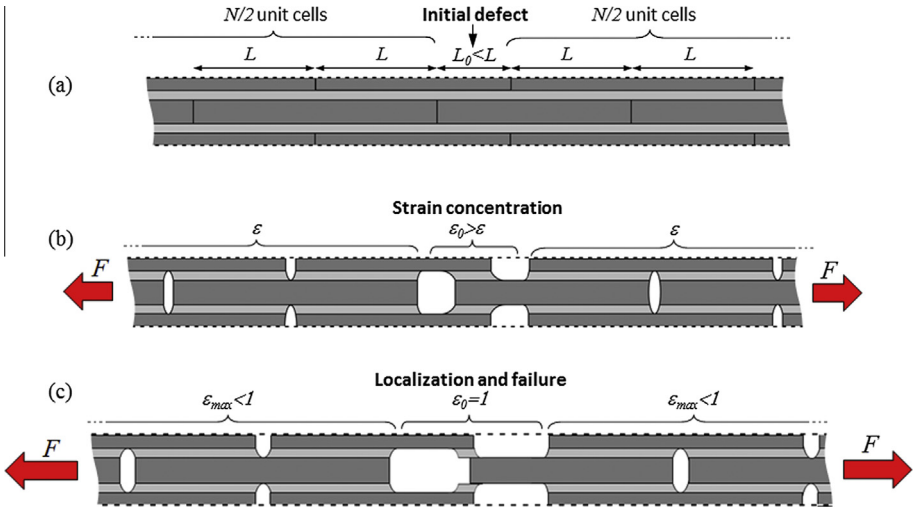

Fig. 5. (a) Chain of N unit cells with overlapcontaining an initial "defect" where the overlap is $L_0 < L$; (b) under tension, the strain is higher at the location of the defect; (c) eventually the model fails at the defect ($\varepsilon_0 = 1$), while the rest of the material undergoes a maximum strain $\varepsilon_{max} < 1$.

In the absence of strain hardening or strain rate hardening (perfect plasticity), only the defect region will yield and the material will localize at the central region of the model. This is a detrimental case which leads to a brittle mechanical response. We now examine the conditions necessary to delay or even suppress localization in the presence of the defect. Following the previous section, the interfaces are modeled with a viscoplastic hardening material:

$$\begin{aligned} \tau &= K\gamma^m\dot{\gamma}^n \\ \tau_0 &= K\gamma_0^m\dot{\gamma}_0^n \end{aligned} \tag{14}$$

with the shear strains and strain rates at the interfaces defined as:

$$\begin{aligned} \gamma &= u/t_i \\ \gamma_0 &= u_0/t_i \end{aligned} \tag{15}$$

These can also be written:

$$\begin{cases} \gamma = \frac{\phi}{1-\phi}\rho\varepsilon \\ \gamma_0 = \frac{\phi}{1-\phi}\rho_0\varepsilon_0 \end{cases} \text{ and } \begin{cases} \dot{\gamma} = \frac{\phi}{1-\phi}\rho\dot{\varepsilon} \\ \dot{\gamma}_0 = \frac{\phi}{1-\phi}\rho_0\dot{\varepsilon}_0 \end{cases} \tag{16}$$

Combining Eqs. (10), (13), (14) and (16) gives:

$$(1-\varepsilon)\varepsilon^m\dot{\varepsilon}^n = (1-\eta)^{m+n+1}(1-\varepsilon_0)\varepsilon_0^m\dot{\varepsilon}_0^n \tag{17}$$

In order to eliminate the strain rate terms, we use $\dot{\varepsilon} = \frac{d\varepsilon}{dt}$ and $\dot{\varepsilon}_0 = \frac{d\varepsilon_0}{dt}$ to obtain the incremental form:

$$(1-\varepsilon)^{1/n}\varepsilon^{m/n}d\varepsilon = (1-\eta)^{\frac{m+n+1}{n}}(1-\varepsilon_0)^{1/n}\varepsilon_0^{m/n}d\varepsilon_0 \tag{18}$$

Eq. (18) is then integrated using the initial conditions $\varepsilon(0)$ and $\varepsilon_0(0) = 0$:

$$\int_0^{\varepsilon}(1-s)^{1/n}s^{m/n}ds = (1-\eta)^{\frac{m+n+1}{n}}\int_0^{\varepsilon_0}(1-s)^{1/n}s^{m/n}ds \tag{19}$$

Eq. (19) can be used to compute the tensile strain ε in the bulk of the material as a function of the tensile strain ε_0 in the defect region. Note that for the extreme case $\eta = 0$ there is no defect and Eq. (19) correctly predicts $\varepsilon = \varepsilon_0$. On the other hand, $\eta = 1$ corresponds to the case where the defect splits the material in half before any load is applied, and in this case Eq. (19) predicts $\varepsilon = 0$. Finally, we note that Eq. (19) does not contain any rate-dependent terms, with the important implication that the strain at failure is rate independent. Eq. (19) was integrated numerically to compute the tensile strain in the bulk of the material ε as a function of the strain in the defect region ε_0, and Fig. 6 shows the effects of m, n and η on the evolution of strains. Failure occurs in the defect region and therefore when the material is stretched to failure the strain at the defect goes from $\varepsilon_0 = 0$ (initial configuration) to $\varepsilon_0 = 1$ (failure at the defect region). The results show that in the early stages of deformation the strains in the defect and in the rest of the material are the same, but they eventually diverge from one another with $\varepsilon < \varepsilon_0$ as the deformations localize. Fig. 6a shows the response of the material in the presence of a relatively large defect ($\eta = 0.1$) and with strain rate hardening ($n = 0.1$). As expected, the strain at failure increases with interfaces with more strain hardening. Fig. 6b shows that strain rate hardening has a similar effect on distributing strains and can be a powerful approach to increasing the ultimate strain of the material. This result will be further developed and discussed in the rest of the article. Finally, Fig. 6c shows the effect of the severity of the defect η. For $\eta = 0$ the strain is uniform throughout the material (no strain concentration) and $\varepsilon = \varepsilon_0$. However, the ultimate strain for the material drops significantly when a defect is introduced: the model shows that, for the set of material properties shown here ($m = n = 0.1$), η as small as 10^{-4} results in a ~50% loss of strain at failure for the material.

The maximum value of ε therefore represents the strain at failure for the entire material, and can be used to assess whether the material is brittle or ductile. Fig. 7 shows ε_{max} as a function of m and n and for a relative defect size $\eta = 0.1$ (results for other defect sizes are not shown here, but they show the same trends as the functions of m and n).

For $m = 0$ and $n = 0$, localization is immediate and the material does not produce any deformation ($\varepsilon_{max} = 0$), which corresponds to brittle behavior. The ultimate strain can be increased by increasing the strain hardening and/or by increasing strain rate hardening at the interface, the highest strains at failure occurring when both mechanisms operate simultaneously. High strains at failure can be obtained, as expected, from pure strain hardening ($m > 0$, $n = 0$) but also, more unexpectedly, from pure strain rate hardening ($m = 0$, $n > 0$). This result implies that an interface behaving as a viscous rheological fluid may produce sufficient strain rate hardening to spread deformations in the presence of defects. The values $m = 0$ and $n > 0$ correspond to a viscous fluid, which is dilatant for $n > 1$ and thinning for $n < 1$. The case $m = 0$ and $n = 1$ represents a Newtonian fluid where K is the viscosity. Interestingly, if $m = 0$, a closed form solution for the ultimate strain can be obtained from (17):

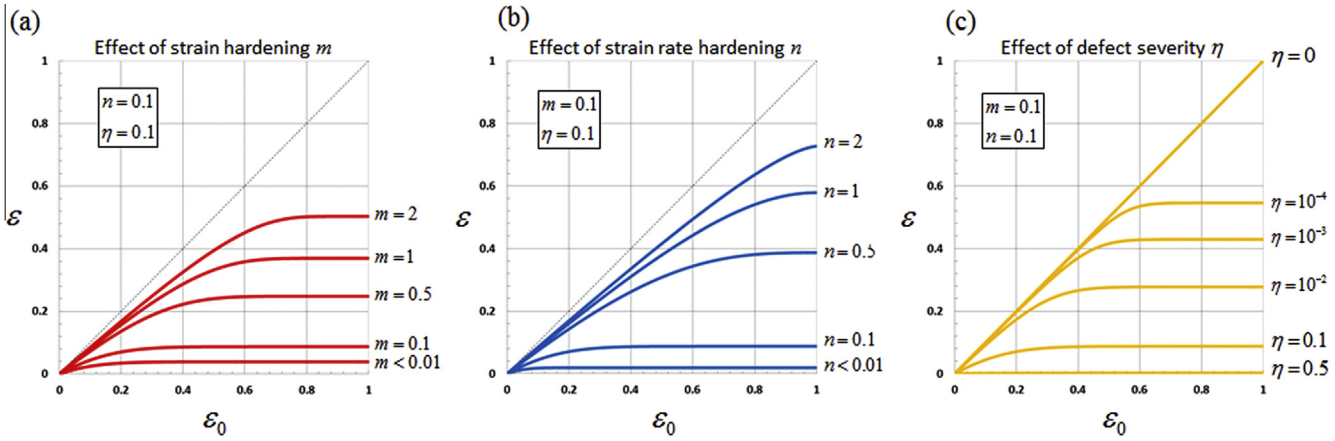

Fig. 6. Tensile strain in the material as function of strain in the defect region: effects of m, n and η.

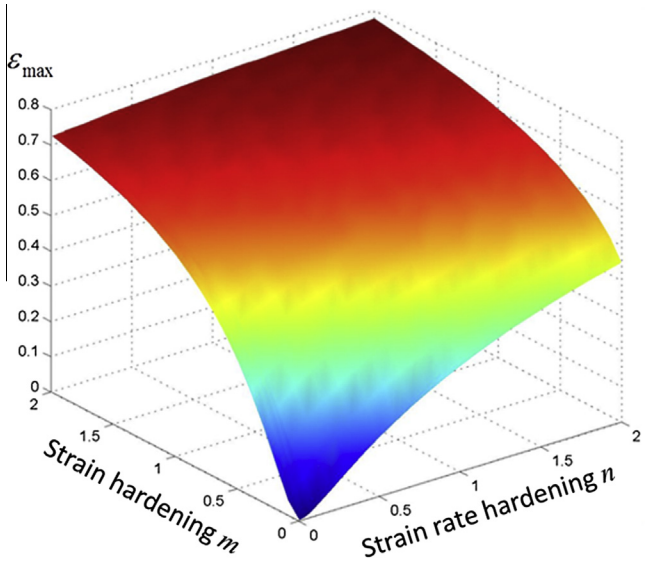

Fig. 7. Ultimate strain as a function of m and n and for $\eta = 0.1$.

$$(1-\varepsilon_0)\dot{\varepsilon}_0^n = \frac{1}{(1-\eta)^{n+1}}(1-\varepsilon)\dot{\varepsilon}^n \tag{20}$$

which, after some manipulations, can be written as:

$$\int_0^{\varepsilon_0}(1-t)^{1/n}dt = \frac{1}{(1-\eta)^{\frac{n+1}{n}}}\int_0^{\varepsilon}(1-t)^{1/n}dt \tag{21}$$

Straight integration gives:

$$\varepsilon = 1-\left(1-(1-\eta)^{\frac{n+1}{n}}\left[1-(1-\varepsilon_0)^{1+1/n}\right]\right)^{\frac{n}{n+1}} \tag{22}$$

The material fails when $\varepsilon_0 = 1$ and therefore the maximum strain in the material is:

$$\varepsilon_{max} = 1-\left[1-(1-\eta)^{\frac{n+1}{n}}\right]^{\frac{n}{n+1}} \tag{23}$$

Note, again, that $\varepsilon_{max} = 1$ only if $\eta = 0$ (no defect). For a Newtonian liquid with $n = 1$, Eq. (23) simplifies to:

$$\varepsilon_{max} = 1-\sqrt{\eta(2-\eta)} \tag{24}$$

Eq. (24) predicts that a complex rheological behavior is not required to achieve strain rate hardening, and that a simple Newtonian fluid at the interfaces is sufficient to spread deformations over large volumes. For example, Eq. (24) predicts that a material with Newtonian fluid at the interfaces and containing a relatively large defect with $\eta = 0.1$ has a strain at failure $\varepsilon_{max} = 0.56$. More generally, the results above highlight strain rate hardening as a powerful mechanism for staggered composites, with profound implications in the mechanics of natural and biomimetic staggered composites. Natural materials such as nacre, bone and spider silk exhibit significant rate dependence, because their interfaces are rich in rate-dependent proteins [1,13,20,29]. Strain rate hardening could therefore play a significant role in generating large deformations and damage tolerance. It is, however, difficult to assess the role of strain rate hardening in these materials, because elastic and strain hardening components also contribute to the overall response. In this work we therefore took another approach to validate the results of our model, where we fabricated and tested a "model staggered composite material". The experiments focused exclusively on the effects of strain rate hardening, and therefore a viscous fluid was used as the interfaces.

4. A model composite material with viscous interfaces: fabrication, testing and modeling

The goal of this section was to confirm experimentally that strain rate hardening is by itself sufficient to spread deformations over large volumes and to promote energy dissipation. To this end, we fabricated a model material with a nacre-like microstructure made of millimeter size glass tablets held together by a highly viscous polydimethylsiloxane (PDMS) at the interface. An ultrahigh-molecular-weight PDMS (UHMW-PDMS) was purchased from Clearco Products Co. (Bensalem. Inc. PA, USA). This PDMS is made of very long polymeric chains which are not cross-linked, so the material behaves like a fluid with very high viscosity [24]. PDMS also has a good chemical affinity with glass, ensuring good adhesion between the PDMS film and the glass tablets. The viscosity of the UHMW-PDMS was measured using a TA Instruments AR 2000 parallel plate rheometer under a controlled shear rate with a frequency sweep of 0.02–100 Hz, corresponding to a range of shear rates of 3×10^{-4}–10^{-1} s^{-1}. The radius of the parallel plates was 12.5 mm and the gap between the plates was set to 1 mm for all tests. The tests were performed at a temperature of 25 °C. The result of the rheological tests (Fig. 8a) show a viscosity in the 20 kPa s range, with a slight decrease in viscosity with shear rate ("shear thinning" behavior). The viscosity $\mu = \tau/\dot{\gamma}$ was fitted with a power law over the strain rates examined (10^{-3}–10^{-1} s^{-1}), giving $\mu = 15{,}345\ \dot{\gamma}^{-0.05}$ (with $R^2 = 0.84$). The parameters for the constitutive Eq. (1) were then $K = 15{,}345$, $m = 0$ and $n = 0.95$. The uncross-linked PDMS therefore exhibits a quasi-Newtonian

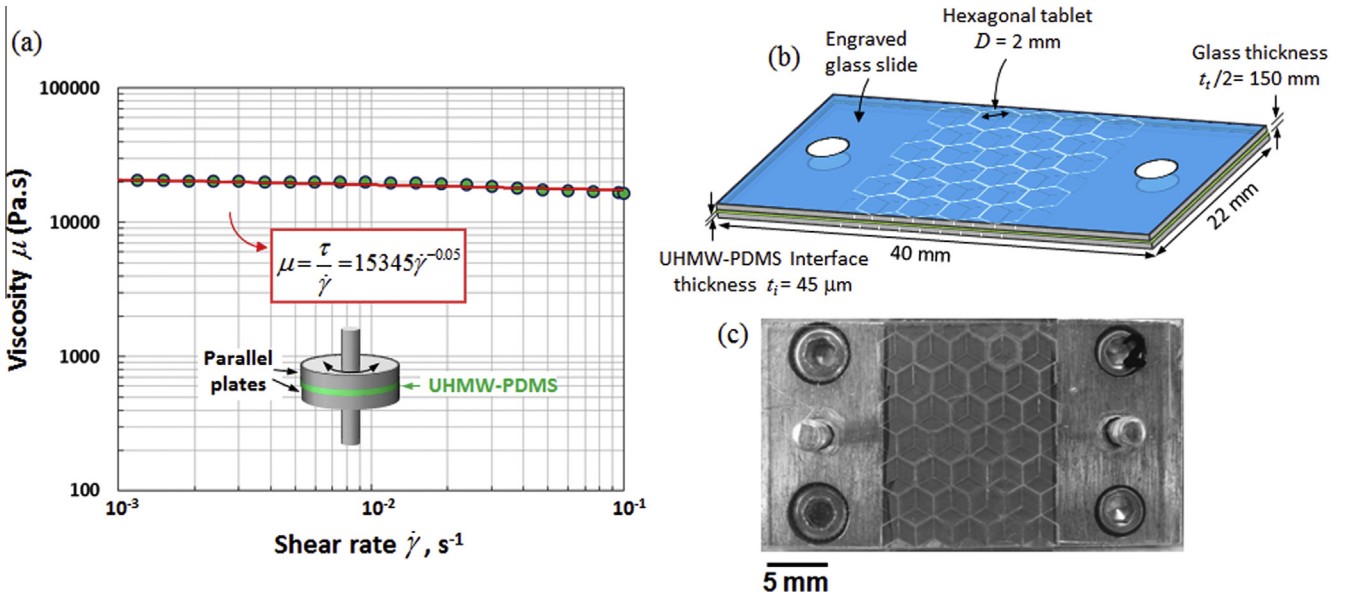

Fig. 8. (a) Viscosity as function of shear rate at room temperature (25 °C) for the UHMW-PDMS used here; (b) sample geometry; (c) actual sample mounted in the loading machine.

behavior over this range of strain rates. The hard tablets were fabricated by cutting hexagonal patterns in thin borosilicate glass slides (22 × 40 mm, 150 μm thick) with a three-dimensional laser engraver (Vitromark, Germany), following a method described in Ref. [30]. Periodic patterns of hexagons with a size D = 2 mm were engraved across the width of the glass slide, as shown in Fig. 8b. The assembly of the model material started by applying a small amount of PDMS mixed with microscopic glass beads 30–50 μm in diameter (99 wt.% PDMS and 1 wt.% beads) between two engraved glass slides. The assembly was pressed together, and the glass beads in the PDMS ensured that the interface was of uniform and well-controlled thickness. Independent experiments (not shown here) showed that 1 wt.% of glass beads was sufficiently small not to affect the mechanical response of the interface. The engraving and the assembly of the two glass slides was designed to generate overlap between the hexagons of the upper and lower slides, generating a staggered arrangement for the hexagonal plate (Fig. 8b and c). Two pinholes were finally cut with the laser at the ends of the sample, in order to transmit tensile forces with the miniature tensile testing machine. The final sample (Fig. 8c) consisted of a two-layer nacre-like structure with stiff hexagonal glass tablets of thickness $t_t/2$ = 150 μm held together by a t_i = 45 ± 3 μm thick layer of UHMW-PDMS. The corresponding tablet concentration was ϕ = 0.87.

The nacre-like glass–UHMW-PDMS composite samples were tested under tension using a miniature loading stage (Ernest F. Fullam Inc., Latham, NY) equipped with a linear variable differential transformer and a 0.2 N load cell. During the test, high-resolution images of the samples were captured at regular time intervals. Samples were tested at a "slow" strain rate of $\dot{\varepsilon} = 3 \times 10^{-4}\ s^{-1}$ and a faster strain rate of $\dot{\varepsilon} = 3 \times 10^{-3}\ s^{-1}$. Fig. 9a shows a set of tensile stress–strain curves obtained at these two different strain rates. The curves initially show a rapid rise in stress with strain up to a peak stress, followed by a gradual decrease to zero stress at $\varepsilon_{max} \approx 1$, which we considered to be the failure point for the material. The initial sharp increase in the stress was attributed to a possible transient response of the interface and to the PDMS flowing within the junctions between the tablets (gaps between the hexagonal tablets belonging to the same layer). As the tablets separated, the junctions played a lesser role and the response was dominated by the interfaces. Stresses were higher for the samples tested at higher strain rates because the response of the composite is governed by the viscous response of the interface. The overall shape of the curve was however the same at the slow and fast strain rates. The stress-softening behavior observed on the stress–strain curves following the transient peak stress is consistent with the model (Fig. 4, viscous fluid case) and can be explained by geometric softening. However, despite this continuous decrease in stress, snapshots of deforming samples at two different strain rates (Fig. 9b and c) clearly show that the sliding of the tablets spread over the entire sample, ensuring a quasi-uniform distribution of deformation within the material. To compare the experimental results with the model, we use Eq. (25), since the interface is a Newtonian fluid. Eq. (25) predicts $\varepsilon_{max} = 1$ since $\eta = 0$ (defect-free material), in agreement with the experiment. Moreover, the amount of spreading in the material does not appear to change with strain rate, which is also consistent with the predictions of the model. We finally verify that in these experiments the glass tablets can be considered rigid compared to the PDMS interfaces. The maximum stress experienced by the composite material is 20 kPa (Fig. 9a). Considering that the tensile stress in the tablets is roughly twice the tensile stress in the tablets (Fig. 3), the maximum stress experienced by the glass tablets is ~40 kPa. Considering the modulus of glass at ~60 GPa, the maximum strain in the glass tablets is $\sim 7 \times 10^{-7}$. Now looking at the interfaces, using Eq. (6) with $\varepsilon \approx 0.05$ (tensile strain at the peak stress), ϕ = 0.87 and $\rho \approx 13$ from the geometry of the hexagon gives $\gamma \approx 4$, which are very large strains since the PDMS essentially behaves like a fluid at the interface. The deformations at the interfaces are therefore seven orders of magnitude larger than in the glass tablets, so that the tablets can be assumed to be rigid compared to the interfaces.

5. Model composite material with a defect

Our final experiment was to investigate the tensile behavior of a staggered composite governed by a viscous response and containing a large defect of controlled size and geometry. The type of sample we used was the same as above, but we introduced a large

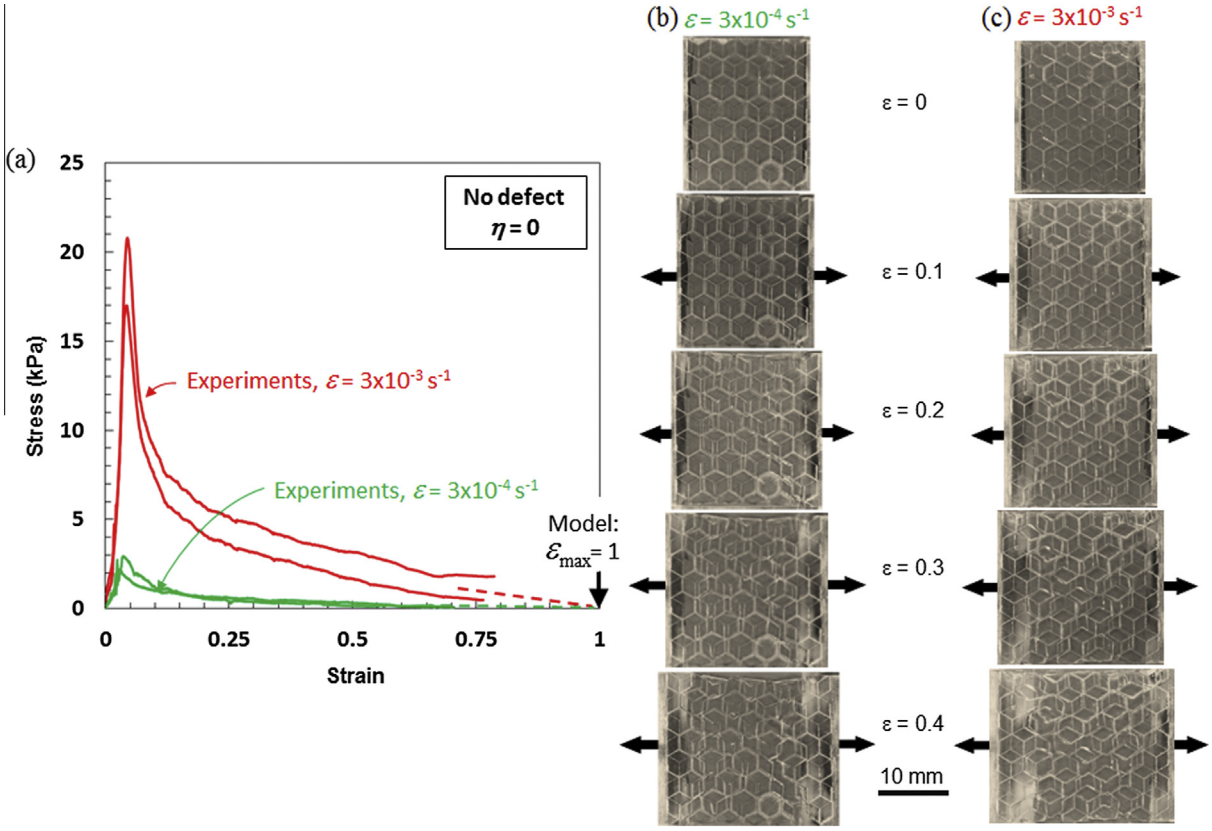

Fig. 9. (a) Stress–strain curves of staggered composite with $\eta = 0$ (no defect); (b, c) sequential images of the sample (top view) showing the deformation mode at two different strain rates.

defect by removing one tablet from the top layer (Fig. 10b and c). These samples were tested in tension using exactly the same procedure as above. The corresponding stress–strain curves had shapes similar to the sample with no defect, but the strength was slightly less (because of the stress concentration at the defect) and the strain at failure was significantly lower (because of the strain concentration at the defect).

Imaging of the deforming sample (Fig. 10b and c) showed a larger strain in the area of the defect, but also showed that large strains were not confined to the defect region, but instead spread throughout the entire sample. This experiment confirmed that strain rate hardening can lead to large deformations even in the presence of a large defect. This behavior was observed at both the slow and fast loading rates, confirming that the evolution of strain around and away from the defect is a rate-independent process. Referring to Fig. 9, the intact sample tested here contained seven overlap regions across the width. After removing the hexagon there are only six overlap regions across the width in the defect region, corresponding to a defect severity of $\eta = (7-6)/7 = 0.14$. With the value $n = 0.95$ from the parallel plate experiment, Eq. (25) predicts $\varepsilon_{max} = 0.49$. Referring to Fig. 5, the number of unit cells along the RVE is N. As discussed above, $N \gg 1$ for actual materials where the microstructure size is much smaller than the size of the component, but this condition does not apply to our model material where $N = 10$. In this case, the contribution of the defect region to the total elongation of the sample u_T must be taken in account, with:

$$u_T = Nu + u_0 \tag{25}$$

where u is the elongation of each unit cell in the bulk of the material and u_0 is the elongation at the defect region. Using Eq. (25) together with Eqs. (10) and (12) gives the macroscopic strain in the material:

$$\varepsilon_T = \frac{\varepsilon}{1+(1-\eta)/N} + \frac{\varepsilon_0}{1+N/(1-\eta)} \tag{26}$$

The macroscopic strain at failure $\varepsilon_{T\max}$ was computed using Eq. (26) with $\varepsilon = \varepsilon_{max}$ and $\varepsilon_0 = 1$:

$$\varepsilon_{T\max} = \frac{\varepsilon_{max}}{1+(1-\eta)/N} + \frac{1}{1+N/(1-\eta)} \tag{27}$$

Using $\varepsilon_{max} = 0.49$, $\eta = 0.14$ and $N = 10$ gives $\varepsilon_{T\max} = 0.52$. This predicted value is very close to the strain at failure measured experimentally (Fig. 10). The assumption that the PDMS behaves as a Newtonian fluid (i.e. constant viscosity and $n = 1$) leads to very similar results: Eqs. (26) and (27) predict $\varepsilon_{T\max} = 0.53$, which differs from the result above by only 2%. The slight shear thinning behavior of the PDMS we used at the interface therefore had little impact on the strain at failure for the composite. The combination of model and experiments therefore confirms that strain rate hardening is a powerful mechanism to minimize the impact of defects as well as to increase the strain at failure and energy dissipation. No particular rheology is required at the interface, and the strains at failure were rate-independent.

6. Summary and conclusions

Nacre, bone and spider silk possess remarkable combinations of strength, toughness and hardness. In particular, the staggered structure of these materials generates unique nonlinear mechanisms which lead to large deformations, energy absorption and toughness [4,11,13,22,31]. The question of how the mechanisms occurring at the nano- and microscales spread over large volumes to translate into high performance at the macroscale is of tremendous importance, yet it has so far received little attention. Here we

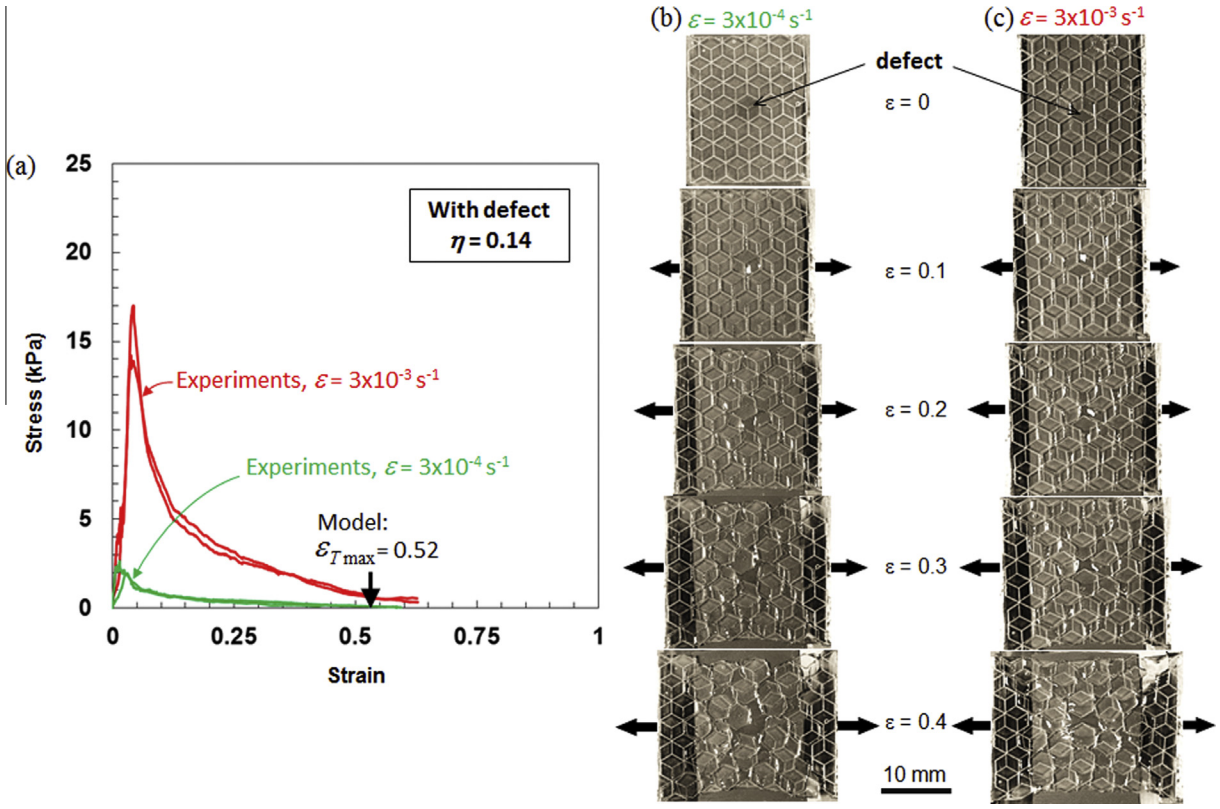

Fig. 10. (a) Stress–strain curve of staggered composite with $\eta = 0.14$; (b, c) sequential images of the sample (top view) at two different strain rates showing deformation with increasing strain.

have developed a model which examines the conditions for large deformations in staggered composites. In particular, the model predicts the macroscopic tensile strain at failure for the material as a function of the viscoplastic parameters at the interface and of the size of the defect. As expected, larger strains can be achieved with strain hardening at the interface. More unexpectedly and interestingly, the model suggested that strain rate hardening can also be a powerful source of large deformations for staggered composites. The model assumes that the tablets are rigid compared to the interfaces, with the implication that the shear strain is uniform along the overlap area. This assumption is verified for natural nacre [28] and for the model material we presented here. It should also be generally valid or at least acceptable for biological and biomimetic staggered composites, since their interface is generally significantly softer and weaker than the tablets [20,28,29]. Incorporating the elastic deformations of the tablets in the model may increase its accuracy, but will probably not change our results significantly since the main source of strains for natural and biomimetic composites comes from the sliding of the tablets on one another. The accuracy of the model may also be improved by considering the three-dimensionality of the real staggered structures and of the defect they contain. These models would rely on accurate descriptions of the three-dimensional configurations of the defects, and would probably require numerical approaches to capture the three dimensional strain fields around these defects. The simple one-dimensional model we present here is however probably sufficient to inform the choice of viscoplastic material for the interfaces in relation to existing defects in the material. Experiments with a glass–PDMS nacre-like staggered composite confirmed that strain rate hardening at the interface can be sufficient to generate large deformations even in the presence of defects, and validated the model in terms of strength and strain at failure. Notably, no special rheology such as shear thickening is required at the interface to achieve this behavior (the PDMS we used, although highly viscous, behaves almost like a simple Newtonian fluid), and the phenomenon is rate independent. This finding has important implications for collagen, bone, nacre and spider silk. These materials are all composed of stiff and elongated inclusions (single proteins, mineral plates or stiff protein crystals) embedded in softer matrices. They display strong rate-dependent mechanical responses [22,32,33], and strain rate hardening could therefore play an important role in delaying failure in these materials. While these materials display a powerful mechanism at the level of the unit cell, it is the distribution of strains which translates these micromechanisms into high properties at the macroscale: energy absorption, large deformation at failure, toughness and tolerance to initial defects and to damage accumulated from excessive or repeated loadings. Strain rate hardening should also be harnessed and optimized in bio-inspired composites, in order to maximize their overall performance.

Acknowledgements

This work was supported by a NSERC Discovery Grant and a NSERC Discovery accelerator supplement. A.K.D. was partially supported by a McGill Engineering Doctoral Award (MEDA). S.B. was partially supported by a Summer Undergraduate Research in Engineering Award from the Faculty of Engineering at McGill. Finally, the authors thank Professor Pascal Hubert for access to the rheometer and Lucie Riffard for help with this equipment.

Appendix A. Figures with essential colour discrimination

Certain figures in this article, particularly Figs. 1–10, are difficult to interpret in black and white. The full colour images can be found in the on-line version, at http://dx.doi.org/10.1016/j.actbio.2014.08.027.

References

[1] Cranford SW, Tarakanova A, Pugno NM, Buehler MJ. Nonlinear material behaviour of spider silk yields robust webs. Nature 2012;482:U72–91.
[2] Fratzl P, Weinkamer R. Nature's hierarchical materials. Prog Mater Sci 2007;52:1263–334.
[3] Zhu D, Ortega CF, Motamedi R, Szewciw L, Vernerey F, Barthelat F. Structure and mechanical performance of a "modern" fish scale. Adv Eng Mater 2012;14:B185–94.
[4] Jackson AP, Vincent JFV, Turner RM. The mechanical design of nacre. Proc R Soc Lond 1988;234:415–40.
[5] Currey JD, Taylor JD. The mechanical behavior of some molluscan hard tissues. J Zool (London) 1974;173:395–406.
[6] Wegst UGK, Ashby MF. The mechanical efficiency of natural materials. Philos Mag 2004;84:2167–81.
[7] Barthelat F, Mirkhalaf M. The quest for stiff, strong and tough hybrid materials: an exhaustive exploration. J R Soc Interface 2013;10:20130711.
[8] Wang RZ, Suo Z, Evans AG, Yao N, Aksay IA. Deformation mechanisms in nacre. J Mater Res 2001;16:2485–93.
[9] Espinosa HD, Rim JE, Barthelat F, Buehler MJ. Merger of structure and material in nacre and bone – perspectives on de novo biomimetic materials. Prog Mater Sci 2009;54:1059–100.
[10] Gao HJ. Application of fracture mechanics concepts to hierarchical biomechanics of bone and bone-like materials. Int J Fract 2006;138:101–37.
[11] Barthelat F, Rabiei R. Toughness amplification in natural composites. J Mech Phys Solids 2011;59:829–40.
[12] Rabiei R, Bekah S, Barthelat F. Failure mode transition in nacre and bone-like materials. Acta Biomater 2010;6:4081–9.
[13] Gupta HS, Seto J, Wagermaier W, Zaslansky P, Boesecke P, Fratzl P. Cooperative deformation of mineral and collagen in bone at the nanoscale. Proc Natl Acad Sci USA 2006;103:17741–6.
[14] Jäger I, Fratzl P. Mineralized collagen fibrils: a mechanical model with a staggered arrangement of mineral particles. Biophys J 2000;79:1737–46.
[15] Kotha SP, Li Y, Guzelsu N. Micromechanical model of nacre tested in tension. J Mater Sci 2001;36:2001–7.
[16] Barthelat F, Tang H, Zavattieri PD, Li CM, Espinosa HD. On the mechanics of mother-of-pearl: a key feature in the material hierarchical structure. J Mech Phys Solids 2007;55:225–444.
[17] Evans AG, Suo Z, Wang RZ, Aksay IA, He MY, Hutchinson JW. Model for the robust mechanical behavior of nacre. J Mater Res 2001;16:2475–84.
[18] Smith BL, Schaeffer TE, Viani M, Thompson JB, Frederick NA, Kindt J, et al. Molecular mechanistic origin of the toughness of natural adhesives, fibres and composites. Nature (London) 1999;399:761–3.
[19] Fantner GE, Hassenkam T, Kindt JH, Weaver JC, Birkedal H, Pechenik L, et al. Sacrificial bonds and hidden length dissipate energy as mineralized fibrils separate during bone fracture. Nat Mater 2005;4:612–6.
[20] Lopez MI, Martinez PEM, Meyers MA. Organic interlamellar layers, mesolayers and mineral nanobridges: contribution to strength in abalone (Haliotis rufescence) nacre. Acta Biomater 2014;10:2056–64.
[21] Bao G. Mechanics of biomolecules. J Mech Phys Solids 2002;50:2237–74.
[22] Buehler MJ, Keten S, Ackbarow T. Theoretical and computational hierarchical nanomechanics of protein materials: deformation and fracture. Prog Mater Sci 2008;53:1101–241.
[23] Hart EW. Theory of the tensile test. Acta Metall 1967;15:351.
[24] Hutchinson JW, Neale KW. Influence of strain-rate sensitivity on necking under uniaxial tension. Acta Metall 1977;25:839–46.
[25] Wang YM, Ma E. Strain hardening, strain rate sensitivity, and ductility of nanostructured metals. Mater Sci Eng A Struct Mater 2004;375:46–52.
[26] Cox HL. The elasticity and strength of paper and other fibrous materials. Br J Appl Phys 1952;3:72–9.
[27] Meyers MA. Dynamic behavior of materials. New York: John Wiley & Sons; 1994.
[28] Barthelat F, Dastjerdi AK, Rabiei R. An improved failure criterion for biological and engineered staggered composites. J R Soc Interface 2013;10.
[29] KhayerDastjerdi A, Rabiei R, Barthelat F. The weak interfaces within tough natural composites: experiments on three types of nacre. J Mech Behav Biomed Mater 2013;19:50–60.
[30] Mirkhalaf M, Dastjerdi AK, Barthelat F. Overcoming the brittleness of glass through bio-inspiration and micro-architecture. Nat Commun 2014;5.
[31] Ritchie RO, Buehler MJ, Hansma P. Plasticity and toughness in bone. Phys Today 2009;62:41–7.
[32] Gosline JM, Guerette PA, Ortlepp CS, Savage KN. The mechanical design of spider silks: from fibroin sequence to mechanical function. J Exp Biol 1999;202:3295–303.
[33] Menig R, Meyers MH, Meyers MA, Vecchio KS. Quasi-static and dynamic mechanical response of haliotis rufescens (abalone) shells. Acta Mater 2000;48:351–5.